# Towards a new generation long trace profiler LTP-2020: Optical design of pencil beam interferometry sensor

P.Z. Takacs[*a], Ian Lacey[b], and Valeriy V. Yashchuk[b]
[a]Surface Metrology Solutions LLC, Minneapolis, MN 55401, [b]Lawrence Berkeley National Laboratory, Advanced Light Source, One Cyclotron Road, Berkeley,CA 94720, USA

## ABSTRACT

Improvements in the quality of synchrotron beamline x-ray optics required for next-generation light sources (e.g. the ALS Upgrade project) drive the need to improve the performance of the metrology instrumentation used to measure these components. The Long Trace Profiler (LTP) that is in use at many synchrotron metrology laboratories around the world has some known issues that affect the accuracy of its measurements. The main error source is optical path difference (OPD) phase error introduced into the probe beam by inhomogeneities in the glass components used in the optical head. We have developed a new optical head design, LTP-2020, that replaces the cube polarizing beamsplitter (PBS) with a thin wedge plate polarizing beamsplitter (WPBS) and replaces the cemented doublet lens with an aspheric singlet. Both of these components significantly reduce the glass volume traversed by the laser probe beam. Careful attention to ghost ray interference produced by back reflection from optical surfaces is necessary to minimize distortion in the primary image that translates into systematic error in the slope angle measurement. We make extensive use of a commercial raytracing program to model the back reflections and adjust component parameters as necessary to minimize distortion. Deliberate misalignment of components is necessary to make the system perform correctly. Stringent requirements are placed on the 45˚ incidence coatings on the WPBS and on the normal incidence coatings on the lens and camera window elements. We encourage our colleagues who wish to upgrade their current LTP systems to join us in the procurement of these custom optical components.

**Keywords**: Long trace profiler, LTP, raytracing, optical design, glass homogeneity, striae, aspheric lens, wedge plate beamsplitter

## 1. INTRODUCTION

As the state of the art in light sources advances (e.g. the ALS Upgrade project), so must the quality of mirrors and the performance of the tools used to characterize them. Despite the existence of world-class tools and current expertise at the Advanced Light Source (ALS) X-Ray Optics Laboratory (XROL) [1] at Lawrence Berkeley National Laboratory (LBNL), planned beamline optical systems have specifications that exceed current measurement capabilities. The tools available to measure these new optics need to be improved to meet the challenge. In particular, the Long Trace Profiler (LTP) has been the subject of a redesign effort to correct some systematic errors that are inherent in the original design [2-4] A previous paper [5] detailed the application of a commercial raytracing program, Zemax OpticStudio®, (ZOS) [6] to solve some of these problems. This work continues the process with a novel optical design that mitigates a major source of systematic error.

## 2. OPTICAL SYSTEM

### 2.1 Lens design

The critical element in the operation of the LTP is the Fourier Transform Lens (FTL). It provides the linear angle-to-position transformation of the probe beam that measures the local surface slope angle. As such, it is effectively known as an F−Theta lens. In order not to introduce systematic error into the measurement, the design of this lens requires the lowest possible distortion over the range of field angles desired. The first commercial version of the LTP, the LTP-II [7,8], produced by Continental Optical Corp. utilized a singlet lens with a focal length of 1250 mm, designed by Jan Hoogland in 1991 [9]. After Ocean Optics acquired the LTP license in 2000, the optical head was redesigned to be more compact with a lens focal length of about 500 mm [10]. In order to have sufficient degrees of freedom to meet the low

*takacs.surfmetsoln@gmail.com phone +1 631.833.0620

distortion requirements, the lens became a more complex cemented doublet. This added 2 extra surfaces and a cement layer between the 2 different glass elements. In order to take advantage of recent developments in optical fabrication technology and to simplify the lens design, we explored the possibility of making the front surface of the lens aspheric and eliminating one of the elements. The result is a singlet lens optimized for low distortion over a field angle range of 40 mrad, i.e. over a surface slope range of 20 mrad (±10 mrad). This is twice the measurement range of the original LTP-II. The material for this lens is fused silica that, unlike the special glasses used in the cemented doublet, can be made with extremely low inhomogeneity.

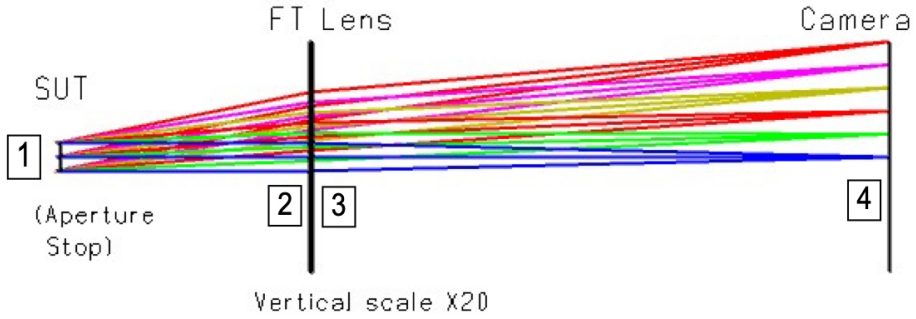


Figure 1. Simplified optical model used in the lens design process. Six field angles used to optimize the lens F-Theta distortion, where image position is a linear function of field angle, ranging from 0 to 20 mrad. Vertical scale is increased by factor of 20 for illustration only. Only 4 objects are required at this stage in the design: 1. Aperture stop at the SUT, 2. Lens front surface, 3. Lens rear surface, and 4. Camera in the focal plane.

Figure 1 is a simplified sequential component (SC) ZOS model of the LTP optical layout used to design the lens. It consists of 4 objects, labeled 1 to 4, that indicate the aperture stop at the surface under test (SUT), the front and back surfaces of the lens, and the camera image plane. Note that the vertical scale of the figure is increased by a factor of 20 to show more clearly the probe beam angles. The aperture stop is located at the footprint of the beam incident on the SUT. The model diagram shows the 2 mm diameter laser probe beams over the 6 field angles emerging from the aperture stop as they encounter the lens and propagate to the camera. Owing to the symmetry about the optical axis, the field angles are shown only over the 0 to +20 mrad range, which corresponds to SUT slope angles of 0 to +10 mrad. The measurement range in the LTP-2020 design has been doubled over the original LTP-II design [11]. Figure 2 shows the F−Theta distortion as a function of field angle over the 0 to 20 mrad range for the optimized lens for 20 Monte Carlo tolerancing runs. The ZOS Tolerancing tool varies both lens radii and the tilt and decenter of each surface according to typical manufacturing tolerances. This gives one an idea of how the final lens product will perform. Compensators for the image plane distance and the lens surface tilts are applied to accommodate the small changes in those parameters that result from the randomly-varied fabrication parameters. The tolerancing result in Fig. 2 shows that the ideal lens will have maximum distortion in the single-digit nanoradian level. The optimized lens parameters are:

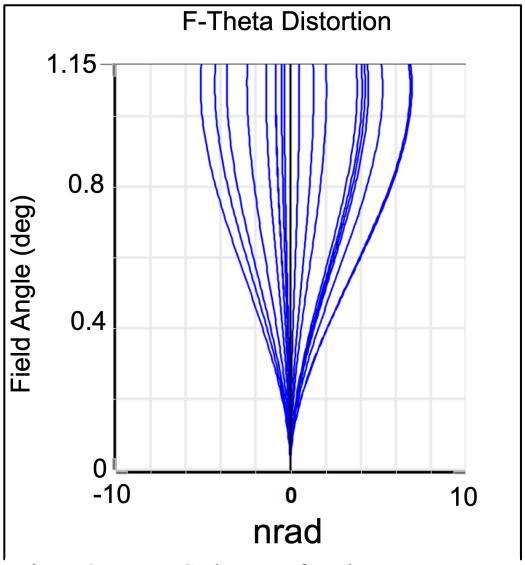


Figure 2. Monte Carlo runs of F-Theta distortion of the 500 mm asphere for random combinations of lens element parameters with typical manufacturing tolerances applied. The maximum distortion at the extreme field angle is less than 10 nrad.

Front surface radius = 867.292 mm CX (convex) with conic constant of -29.314 (hyperbolic),
Rear surface radius = 290.151 mm CX,
Thickness = 9.8 mm.
Glass material is specified to be Suprasil 3001 or 300 with the best possible homogeneity.

## 2.2 Glass Inhomogeneity

Current versions of the Long Trace Profiler have a number of known defects that limit performance. Foremost among these is the glass inhomogeneity problem [12-15]. The probe beam that carries the surface slope error information passes through a thick glass beamsplitter cube twice and then through a cemented doublet lens on its way to the CCD camera. Inhomogeneities and striations in the glass and in the cement layers between the cube and lens elements with characteristic spatial dimensions of 1 mm and below introduce phase shifts within the probe beam that distort the image and produce systematic slope error. Figure 3 shows measurements of apparent microradian-level residual slope errors produced by scanning a laser beam across several cube beamsplitters [8, 15]. A perfect cube would produce an undeviated image spot. One can see that the 3 commercial-quality cubes produce apparent PV slope errors in the range of 10s of microradians. Even the custom-made BS cube (lowest curve) has errors in the range of 1-2 µrad. When the need is to measure the surface quality of mirrors with single-digit nanoradian errors, this level of systematic error is intolerable.

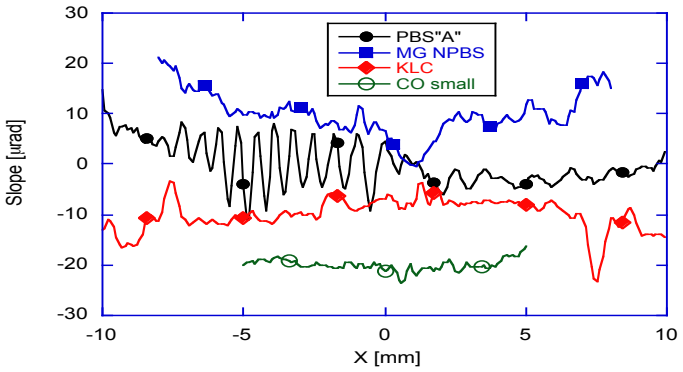


Figure 3. Apparent slope errors produced by scanning a laser beam across various glass cube beamsplitters [8, 15]. The upper 3 are commercial stock items; the lowest curve is a custom made unit for use in an LTP. The best performance still has errors at the microradian level.

Another source of glass error is the quality of the Fourier transform lens (FTL), which is a 14 mm thick cemented doublet in the most recent LTP implementations. A typical transmitted wavefront residual error plot from a Fizeau interferometer measurement is shown in Fig. 4. The rms OPD for this lens is 16.3 nm. This OPD error contributes to the phase error within the laser beam, distorting the image, producing slope error. The plot on the right shows the apparent slope error produced by this surface for a laser beam scanned across the lens at normal incidence with indicated offsets in the orthogonal direction. The PV slope error for each is about 3-4 µrad with an rms error of 0.75 µrad. This shows that a lens with 16.3 nm of OPD error, which is about λ/40 optical quality, needs to have a much tighter wavefront error specification in order to significantly improve the performance of the new system.

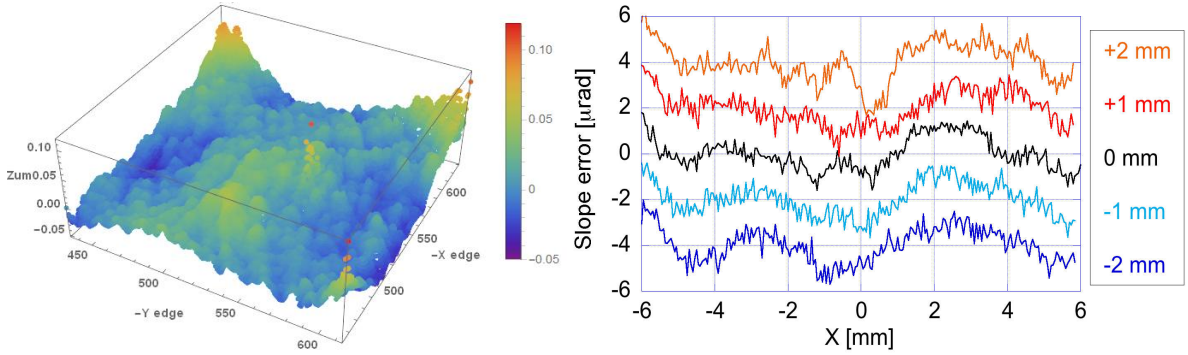


Figure 4. (Left) Fizeau interferometer measurement of transmitted wavefront error for the FTL over 20x20 mm square central region. Vertical scale is in microns. RMS error is 16.3 nrad; (right) Apparent slope error in y-position of laser beam scanned across the lens with the wavefront error shown on the left. Lens is shifted laterally between scans as indicated. Average rms error is 0.75 µrad for each scan.

Using the measured wavefront OPD error, we can simulate image distortion using the physical optics propagation (POP) tool in ZOS. The POP tool propagates wavefronts from element to element in sequential component (SC) design mode. The single-mode Gaussian laser beam, after collimation, has a $1/e^2$ radius of 1.04 mm at the field stop aperture placed at the SUT position. The left frame in Fig. 5 shows the ideal image irradiance of this beam propagated to the focal plane of the Fourier transform lens. The interferogram wavefront is imported into the lens editor as a Grid Phase (GP) surface and is placed onto the lens front surface. The right frame in Fig. 5 shows the y-profile intensity through the center of the images produced by turning on and off a Grid Phase surface corresponding to the measured wavefront scaled to a 1 nm rms phase error. One can see how the distorted image shifts away from the undistorted image by a few microns. A ZOS macro simulates a SUT scan by sending the laser beam through the lens over a range of field angles. The image intensity is binned into one y-profile, and a Gaussian function is fit to the upper half of the y-profile.

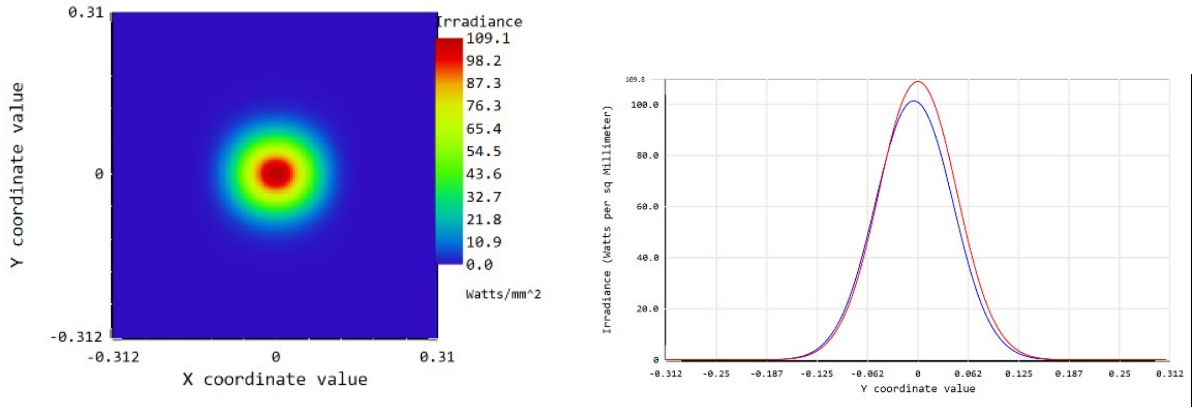


Figure 5. (Left) POP image of ideal laser beam at the detector plane. Axis units are mm. (Right) Y-profiles through the centers of POP images: (red) undistorted beam, (blue) with Grid Phase-produced distortion that shifts the beam by a few microns. Abscissa units are mm.

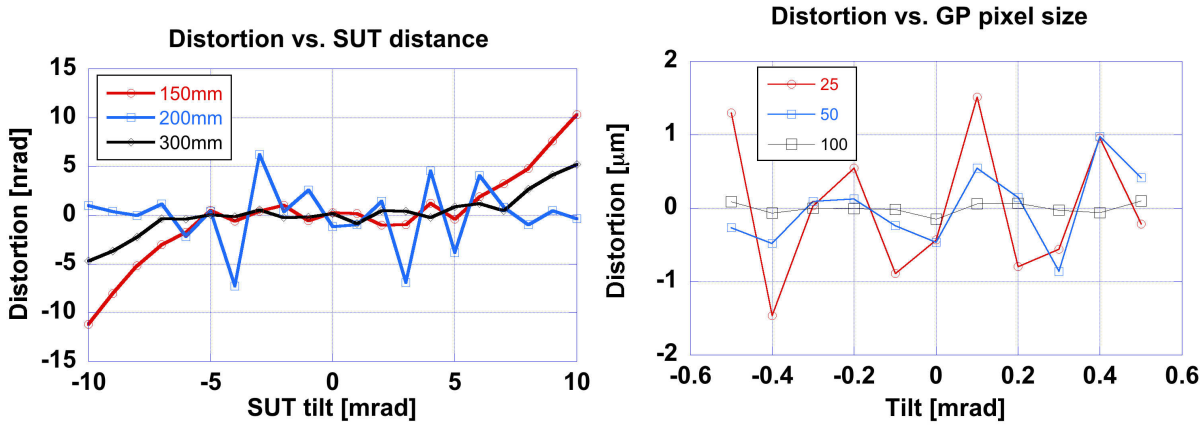


Figure 6. (Left) POP calculation of image distortion as a function of SUT tilt angle for the 3 SUT distances. Deviation from linearity is less than 10 nrad over most of the range; (right) Distortion with the Grid Phase surface added for grid granularity sizes of 25, 50, and 100 µm. The magnitude of the error increases by 3 orders of magnitude for a moderate 1 nm rms wavefront error.

Without the Grid Phase surface, the ideal distortion level is on the order of nanoradians for the 3 SUT distances, shown on the left in Fig. 6. This distortion level was seen in the tolerancing runs earlier. The propagating Gaussian beam picks up phase distortion as it passes through the Grid Phase surface, resulting in a distorted and shifted image in the focal plane. The residuals of a straight-line fit to the mean of each y-profile are plotted and the resulting graphs show the distortion produced by the Grid Phase surface as a function surface slope angle. The three curves on the right in Fig. 6 are for different GP surface pixel sizes. As the granularity in the pixel size increases, the OPD phase error map becomes smoother and the distortion decreases. GP pixel sizes in the range of 25 µm give PV errors of a few microns, in

agreement with the actual laser beam translation measurements shown above in Fig. 4. Recall that the scaling factor for focal plane position and SUT slope error is 1 µm = 1 µrad, or 1 nm = 1 nrad. The magnitude of the distortion, produced by the GP surface scaled to a 1 nm rms wavefront error, increases by 3 orders of magnitude over the ideal case. This indicates that the performance of the LTP will be limited mainly by the quality of the surface figure and finish of the lens and by the glass homogeneity properties, not by the nominal FTL design parameters.

### 2.3 Thin plate polarizing beamsplitter

The major innovation in the LTP2020 optical system is the use of a thin plate polarizing beamsplitter with a 0.5˚wedge angle (WPBS) to replace the thick cube polarizing beamsplitter (PBS). The probe beam no longer passes through any PBS glass on its return from the SUT. This change eliminates the glass inhomogeneity phase error picked up by the probe beam in the old PBS cube. It also allows for the use of N-BK7 as a substrate material instead of more costly striae-free fused silica. The layout of the full LTP-2020 optical system is shown in Fig. 7. The detail on the right shows the probe beam ray segment (3) returning from the SUT to the WPBS, reflecting off the back surface of the WPBS to the FT Lens (4). The only possible phase error that could be added to the probe beam from the WPBS is from surface figure and finish error on the back surface. But this plano surface can be polished easily to sub-nanometer roughness tolerances, much smaller than the level of the glass inhomogeneities, so it will no longer be a significant source of wavefront error. The major issue with the WPBS is the coating requirement. The front surface needs to have an anti-reflection (AR) coating that provides a polarization-independent reflectivity of no more than 0.01% ($10^{-4}$) at a 45˚ incidence angle at a 633 nm wavelength. The back surface needs a narrow-band polarizing coating with an extinction ratio of at least 1:10,000 at 45˚ for 633 nm wavelength. These stringent coating requirements arise from the need to minimize ghost rays produced by multiple reflections from the glass surfaces.

### 2.4 Optical layout

The full LTP-2020 system optical layout is shown in Fig. 7. Figure 7(a) shows the central rays for the SUT and REF arms, with the SUT surface tilted slightly so that its rays are not coincident with the REF arm rays in this view. Figure 7(b) identifies the main beam central ray segments as they pass through the WPBS and the FT Lens. Figure 7(c) is a CAD rendering of all of the optical head components in their mounts, except for the camera. The WPBS is oriented so that its wedge direction is oriented along the x-axis (normal to the plane of the page). This has the effect of deflecting ghost rays (not shown) produced within the wedge away from the main beam central rays, out of the plane of incidence. This reduces interference produced by the WPBS. But the price one pays for this improvement is more complicated laser beam positioning. In order to direct the laser beam exiting the WPBS down to the SUT through the origin of the coordinate system (0,0,0) to be exactly parallel to the Y-axis, the laser source needs to be slightly skewed in position and angle from its nominal on-axis orthogonal position. This is easily accomplished by using the optimization feature of ZOS with the appropriate operands. The final design keeps the back surface of the WPBS coincident with the x-axis and the coordinate system origin, and at an angle of exactly 45˚ to the Y- and Z-axes. The FT Lens is then placed with its optical axis coincident with the Z-axis. The folding mirrors in the optical path following the lens are placed at 45˚ angles to direct the optical axis onto the center of the detector, which will be an sCMOS camera (not shown).

The skewed laser beam and the WPBS wedge angle complicate the design of the reference arm. The purpose of the reference arm is to track the pitch angle errors in the optical head as it is translated along the LTP gantry. The fold mirrors added to the REF arm realign the outgoing REF beam to the z-axis after it exits the WPBS at a skew angle. The basic idea is to make the REF beam exactly parallel to the z-axis (which is the gantry translation axis), keep it stationary on the REF mirror as the optical head is translated along the gantry, return through the center of the FTL, and have its image on the CCD offset by a small amount from the SUT image spot to avoid overlap. However, even with the degrees of freedom introduced by the two fold mirrors, it is not possible to satisfy all of these conditions. The final solution requires that the REF beam walks across the REF mirror surface by about a millimeter as the gantry carriage moves over its 1 meter travel length. This 1 mm movement on the REF mirror should not introduce significant slope error into the measurement, as these fold and reference mirrors are superpolished flat to a sub-nanometer surface finish.

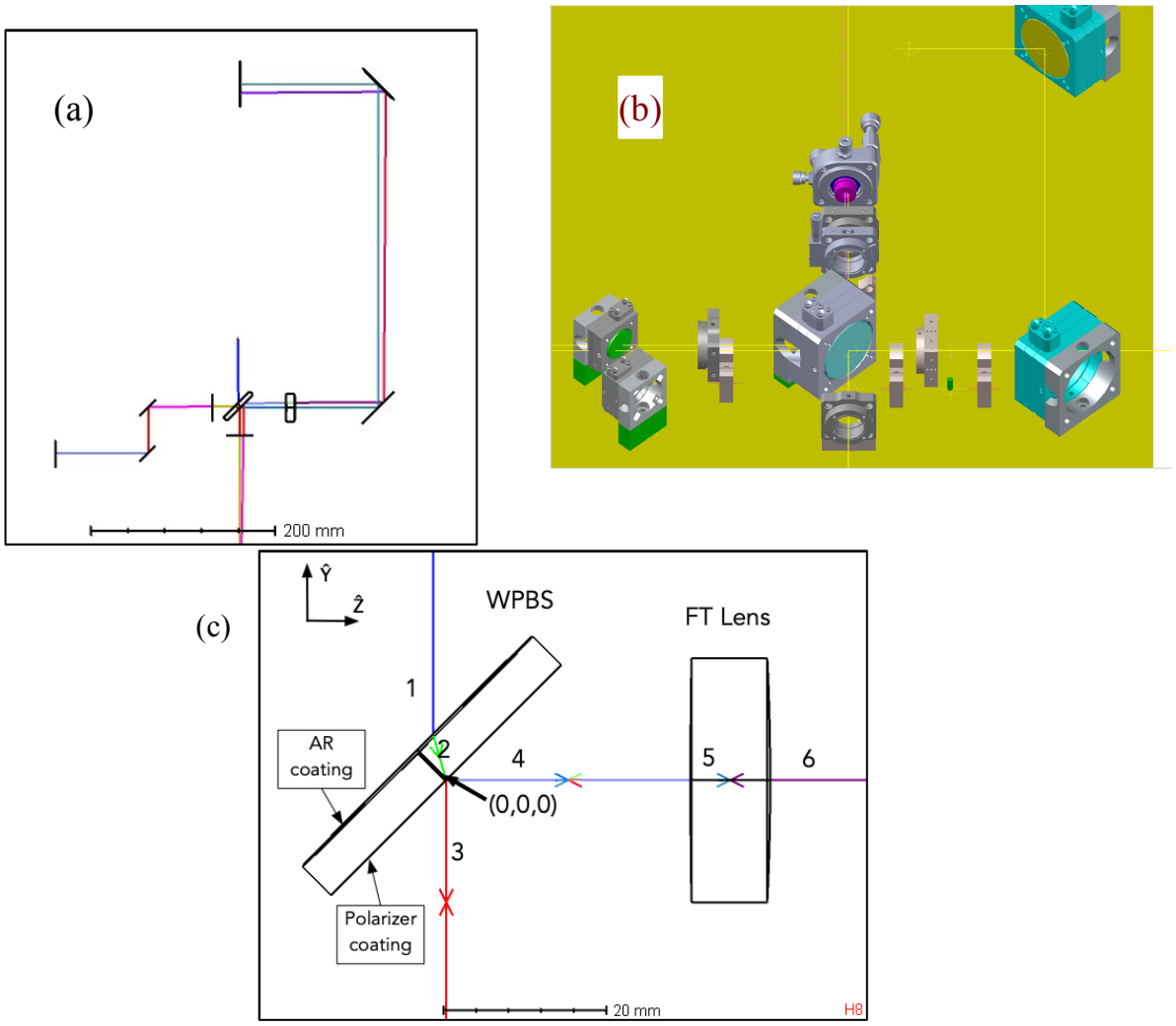


Figure 7. (a) Optical diagram of the new LTP-2020 layout with the WPBS replacing the cube PBS. The SUT is off the bottom of the frame; (b) CAD model rendering showing layout of all optical head components. Not included is the camera; (c) Detail showing the ray paths for rays to and from the SUT. The returning rays reflected from the SUT (3) are reflected from the WPBS (34) without passing through any glass on the WPBS. Only the ray segments inside the FTL (5) are subject to glass OPD error.

### 2.5 Ghost ray mitigation

A major advantage of using a commercial raytrace program in the design of the LTP-2020 is the ability to see the effects of ghost rays produced by reflections from glass surfaces. ZOS tracks each ray segment as it encounters a surface and splits into branch segments by reflection and transmission. It keeps track of the actual intensity in each segment that is affected by the reflectivity of the coating and absorption in the glass medium. It will propagate rays until the ray segment intensity falls below a user-defined minimum relative ray intensity (MRRI) threshold level, which is usually set to be $10^{-6}$ – $10^{-7}$ of the initial ray intensity. The SC mode of ZOS has a Ghost Ray Analysis tool that isolates the various ghost ray sources so they can be analyzed individually. Using the simplified model in Fig. 1, we can isolate the sources of the ghost rays produced by the lens and detector. However, ZOS does not allow one to put a coating on a detector surface, so we must first add a glass element with a flat surface in back of the detector, to which we apply a coating with a 0.5% reflectivity to simulate the estimated CMOS surface reflectivity. This is a best-guess for the sensor, as we don't know the actual properties of the AR coating applied to the CMOS surface. We put an AR coating on both lens surfaces that has 0.01% reflectivity.

Setting a high MRRI threshold, e.g. $10^{-2}$, allows one to see only the main rays along the optical axis of the system, as shown in Fig. 7(a). Lowering the threshold so that we see the ghost rays from lens and camera back reflections, we see that there are 3 major sources of ghost images, shown in Fig. 8. We identify the ray branches by the originating back-reflecting surface and the subsequent forward-reflecting surface. Referring to the element designations in Fig. 1, the 3-2 and 4-3 images are greatly defocused, so they pose no significant interference problem with the main beam. The 4-2 reflection is the most problematic. It arises from a sensor back reflection (4) that again back reflects from the front surface (2) of the lens. The back reflection from the sensor is nearly collimated when it reaches the lens surface, and the back-reflections from the convex lens surface pick up enough curvature to produce a ghost focus at approximately half way to the camera. The resultant image on the sensor has an rms radius of about 1mm, whereas the main beam image radius is about 100 microns. The ghost image is spread out over an area that is 100 times larger than the main beam image. The rays in the ghost image are attenuated relative to the main beam by a factor of $10^{-4}$ from the surface 2 reflection and a factor of $5\times10^{-3}$ from the sensor, for a total attenuation of $5\times10^{-7}$. We need to see if and how this ghost image affects the distortion of the main beam. Note that this ghost image position moves in the direction opposite the main beam as the SUT tilt increases from normal incidence. So, after a SUT tilt of about 1mrad, this ghost image no longer poses a problem.

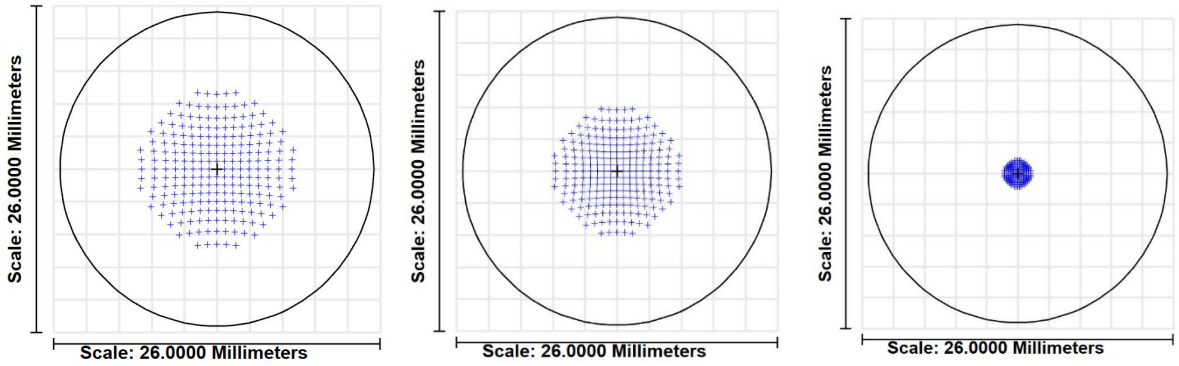


Figure 8. Ghost ray geometric spot diagrams for (from left) the 3-2, 4-3, and 4-2 back reflections. The 4-2 reflection is the worst case for ghost ray interference with the main image spot.

The simplified SC-mode geometric raytrace model, however, does not tell the whole story about ghost rays. It only calculates ghosts between the lens and the sensor. In the full NSC system model that includes the WPBS and the SUT, there are more opportunities for ghosting. In particular, the major source of ghost rays is back reflection propagating between the sensor and SUT. With the SUT at 0˚ tilt (normal incidence), the main beam rays reflect back from the camera to the SUT and back again to the camera. These double-bounce ghost rays have a unique property that they always come to the same focus position on the sensor independent of the SUT tilt angle. The double bounce off the SUT cancels the tilt angle and sends the ghost rays back through the lens parallel to the z-axis. Hence, they form an image exactly at the center of the sensor, which is also where the main beam spot is formed with the SUT at normal incidence. This ghost image stays put as the SUT is tilted, so the only interference is for SUT slopes near 0˚.

To calculate the correct intensity of these rays, one must take into account the polarization rotations provided by traversing the half-wave plate (HWP) and the fold mirror surfaces (Al-coated mirrors) and the polarization ratio of the WPBS (10,000 to 1). ZOS keeps track of all of the electric field components for each ray segment. The result is a ghost image with a peak intensity slightly larger than that of the lens back reflections. But it is focused to a small spot, the same size as the main beam. The only mitigation for these SUT back reflection ghost rays is to rotate the camera surface or lens by a small amount about the y-axis to shift the ghost image away from the center of the detector. A rotation angle of only a few milliradians is sufficient. In fact, this misalignment is more likely than not to happen when the folding mirrors are connected to the optical head during final assembly. Figure 9 shows the NSC layout of the rays onto the detector surface with the lens tilted by 0.35˚. The double bounce ghost image is off the edge of the detector area, which is a 5×5 mm area in this model. The main beam ray bundle is seen converging onto the center of the detector, with the defocused back-reflected rays from the lens surrounding the main image. This is an example of the principle of "deliberate misalignment," necessary to make the system work properly.

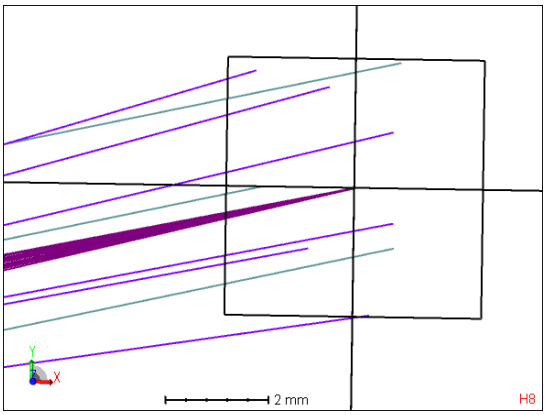


Figure 9. Final configuration with lens rotated by 0.35˚ about the Y-axis to move the SUT double bounce ghost off the detector region. The converging bundle in the center is the main beam image; the single rays surrounding are from the unfocussed lens back reflections. The detector area shown here is 5×5 mm square.

### 2.6 Fresnel diffraction image distortion calculation

To see what the effect a weak ghost image has on the main beam image, a one-dimensional Fresnel diffraction integral was implemented in a Mathematica™ [16] code to model two wavefronts propagating from an aperture with different amplitudes and with a tilt angle between them. This method is based on Huygens construction, where each point in the image is the square of the sum of the phases over all the optical path lengths from every point in the aperture. The expression for the value of an image point, $x_{im,}$ at a distance, z, from the aperture is given by

$$I\left(x_{im}\right)=\left\{\sum \exp\left(-\frac{x_{ap}{}^{2}}{2\sigma^{2}}\right)\left\{A_1\exp\left(i\frac{2\pi}{\lambda}\frac{x^{2}_{ap}}{2f_1}\right)+A_2\exp\left(i\frac{2\pi}{\lambda}\frac{x^{2}_{ap}}{2f_2}\right)\exp\left(\mathrm{i}\frac{2\pi}{\lambda}\theta x_{ap}\right)\right\}\exp\left(i2\pi\frac{\left(x_{im}-x_{ap}\right)^{2}}{2\lambda z}\right)\right\}^{2}$$

where the sum is over all the aperture source points. The expression in the middle brackets is the sum of the direct beam with a converging wavefront with radius $f_1$ = -500 mm and the ghost beam with a different wavefront curvature, $f_2$, and with a tilt angle given by the θ term. The Fresnel diffraction kernel is in the last set of brackets. The first term in brackets describes the amplitude distribution of the incident beam in the aperture. It is the same for both the direct and ghost ray beam in this model. The ratio of the two electric field amplitudes, $A_1$ and $A_2$, depends on the square root of the peak intensities of each image spot. For the current model, with a 0.5% reflective AR coating on the sensor and a high reflectivity coating on the SUT, the intensity ratio is $2\times10^{-6}$ for the double bounce rays. The electric field ratio is then $1.41\times10^{-3}$. This is the worst case ghost ray configuration. The rays that reflect back from the lens have about an order of magnitude lower intensity than the SUT double bounce rays, owing to the better AR coating on the lens surfaces. However, we use the worst case intensity for all of the Fresnel diffraction calculations as an upper limit to the distortion.

The result for the SUT double bounce distortion simulation is shown in Fig. 10. The distortion occurs only when the main beam is near normal incidence on the SUT. As the SUT tilt angle increases, the distortion rapidly goes to zero as the overlap between the two coherent images decreases. Fortunately, this distortion can be eliminated by tilting the lens or camera by less than 0.5˚ in the transverse direction. The other 2 significant distortions are produced by the defocused images from the (4-2) rays that back-reflect from the sensor to the lens front surface (Fig. 11, left) and from the (3-2) rays that bounce back from within the lens (Fig. 11, right). These distortions extend over a larger SUT tilt range because these ghost images are defocused at the camera, as shown in Fig. 8 for the geometric raytrace footprints. The maximum PV distortion from the (4-2) reflections is about 20nrad and from the (3-2) reflections is about half this value. Note that these distortions are an upper limit to the actual values because the reflectivity of the surfaces is overestimated in the simulation.

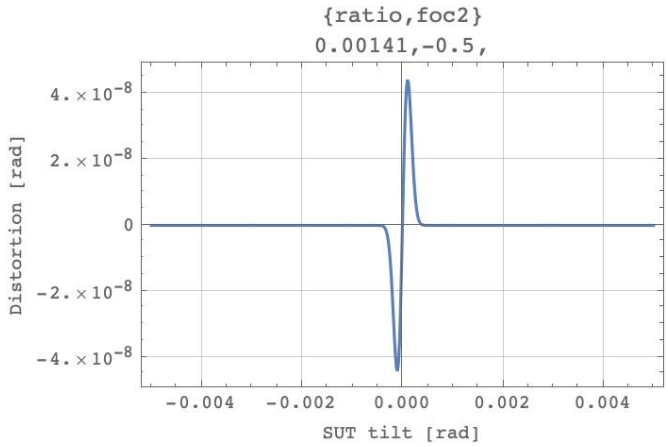


Figure 10. Distortion produced by the SUT double bounce image interfering with the main beam. The PV distortion over the full SUT tilt angle range is about 100 nrad.

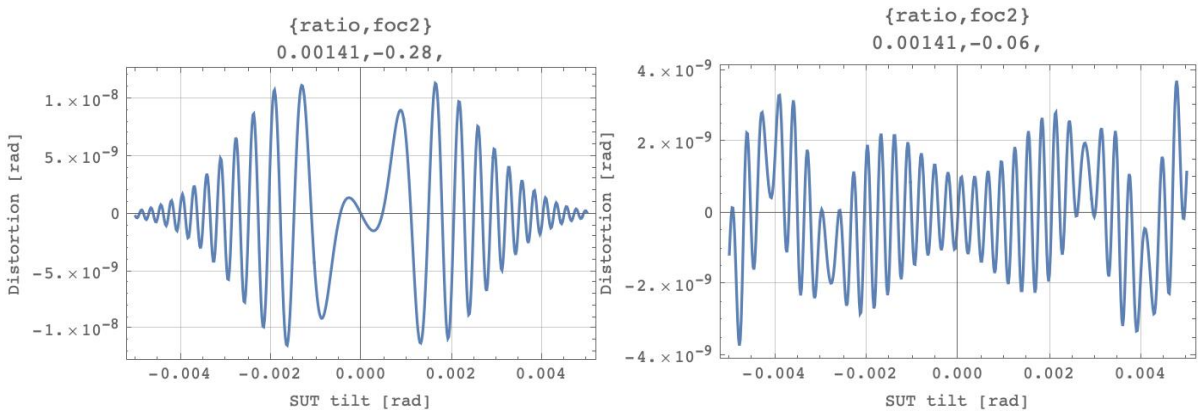


Figure 11. Distortion vs. SUT tilt angle for: (left) the (4-2) detector to lens front surface rays, and (right) the (3-2) lens internal reflections.

The final result of this optical modeling effort is to confirm that the quality of the lens fabrication will be the limiting factor in reducing the systematic error in the optical system. Replacing the cube PBS with the thin plate wedge WPBS eliminates a major source of wavefront irregularity. The multiple reflection distortions can be mitigated with the proper optical coatings and deliberate misalignments.

## 3. FABRICATION ISSUES

### 3.1 Aspheric lens

The specifications on the quality of the lens are very stringent. The distortion results in Fig. 6 indicate that we need wavefront error well below the 1 nm rms level over the sub-mm spatial period region in order to get the distortion below the microradian level. To get down to this nanoradian level is essentially impossible with conventional polishing methods. So we developed a set of specifications that should improve the accuracy of the new LTP by an order of magnitude over the current system and get us down to the few tens of nanoradians level of accuracy. The power spectral density (PSD) specification for the residual wavefront error (after removing the best-fit ideal wavefront) is shown in Fig. 12. The high frequency region, for periods below 2 mm, has an rms error of 0.5 nm. The low frequency region, for periods longer than 2 mm, has a relaxed rms of 2.5 nm, which is λ/250 in terms of wavelength. These specifications are not what most manufacturers will sign up to meet. For this reason, we have had a very difficult time finding a vendor who is willing to try. As of this writing, we have found one vendor and have issued a purchase order for 10 lenses.

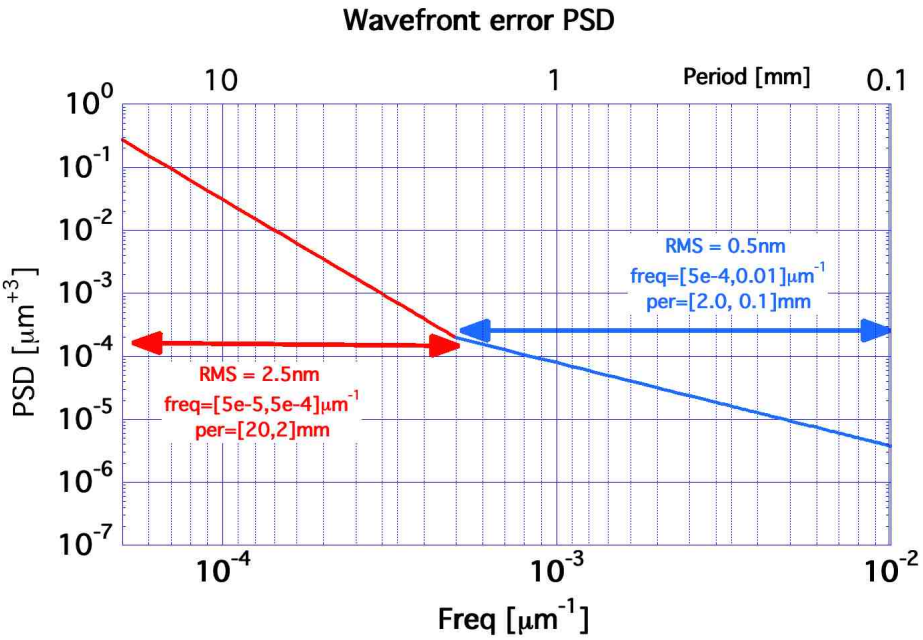


Figure 12. Upper limits for the transmitted wavefront residual error of the lens. The best-fit asphere wavefront has been subtracted.

As an alternative to producing a lens by the usual material removal methods, we are exploring the possibility of producing the aspheric surface by an additive deposition method. The maximum departure of the aspheric surface from a sphere is only 70 nm, so it may be possible to start with a spherical surface and add fused silica to it to produce the desired profile. We will have more to report on this method in the future.

The lens requires an anti-reflection coating with reflectivity less than 0.01% in order to mitigate the ghost ray reflections. Typical AR coatings only give a factor of 10 reduction from the nominal uncoated surface reflectivity of 4%. Our coating vendor has a design for a multilayer coating that will produce a reflectance of better that 0.01% at normal incidence.

### 3.2 Wedge plate polarizing beamsplitter

The WPBS that replaces the 30 mm thick cube PBS is 5 mm thick with a 0.5˚ wedge angle. The material is N-BK7 instead of fused silica, since the return beam from the SUT does not pass through the WPBS and homogeneity of this glass material is no longer an issue. The back surface, however, needs to be super-polished flat and smooth in order not to introduce phase error into the laser probe beam. The front surface only needs a conventional polish, as the reference beam does not move significantly over different regions of this surface. The coating requirements on the two surfaces are, however, very stringent. The AR coating on the front surface needs to have a polarization-independent reflectivity of better than 0.01% at a 45˚ angle of incidence. The polarizing coating on the back surface needs to have a polarization ratio of 10,000:1 at 45˚. Our coating vendor has designs for both coatings that meet or exceed these specifications.

### 3.3 Camera

The camera is a Kinetix sCMOS with a 10 Mpixel back-illuminated sensor. It has a 1 mm thick fused silica window located 10 mm in front of the sensor. The nominal AR coating on this window is a conventional broadband coating that only reduces the back-reflection by about a factor of 10. Distortion results from our NSC model for several AR coatings shown in Fig. 13 indicate that the reflectivity needs to be less than 0.05% to reduce the distortion below the 100 nrad. We specify the AR coating to have a maximum reflectivity of 0.01% ($10^{-4}$) at 633 nm to keep the distortion below the 30 nrad level. One can see that the distortion near normal incidence is very small for any of these curves, but increases significantly as the incident beam angle increases. The peak distortion occurs for an incident beam angle of about 0.6˚, which corresponds to a surface slope angle of about 5 mrad. This would introduce an unwanted systematic error into surface curvature measurements. We are having custom AR coatings applied to the camera windows to reduce the

reflectivity to below 0.01% at 633 nm. The same AR coating that is designed for use on the aspheric lens can be used on these windows, since the material for both is fused silica and is used at normal incidence.

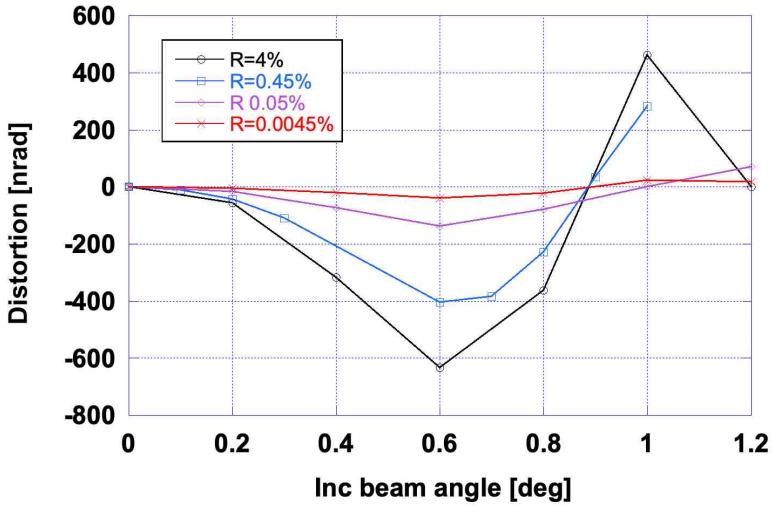


Figure. 13. Distortion produced by camera window back-reflection of rays from the sensor surface for a range of AR coatings with the indicated reflectivities.

## 4. CONCLUSIONS

The optical design presented in this paper achieves the major objective in attempting to reduce the systematic error produced by glass inhomogeneity in LTP optical components. Replacing the cube PBS with a wedge plate polarizing beamsplitter eliminates the OPD error produced by the return beam traversing the glass inside the cube PBS. With the wedge plate, the return beam reflects off of the outside of the back surface – it does not pass through any glass on the WPBS. Since the back surface of the WPBS is plano, it can be polished to be very flat and smooth and will contribute very little to the wavefront error in the return beam. The use of a singlet lens with an asphere applied to one surface also reduces the wavefront error produced by the cemented doublet. The substrate material for the singlet lens is specified to be the highest quality fused silica that has the lowest variation in index of refraction. Ghost rays produced by multiple reflections from the optical surfaces that interfere with the main image to produce distortion need to be controlled by stringent requirements on coatings and by careful misalignment of components. Narrow band AR coatings with reflectivities less than 0.01% are required to minimize ghost ray production. The lens, WPBS, and camera components are currently being ordered. We encourage anyone seeking to upgrade their existing LTP to collaborate with us in the procurement of these custom optical components.

## ACKNOWLEDGEMENTS

The authors acknowledge useful discussions with Dr. Ray Conley regarding the additive deposition method for aspheric lens fabrication. We acknowledge the expertise of Tony Pirera and Derek Schomburg at Spectrum Thin Films, in developing the coatings for the FTL, WPBS, and the camera windows. We are grateful for the assistance of Mic Chaudoir and Jim Schumacher at Teledyne Princeton Instruments with the Kinetix camera customization.

This work was performed in the scope of subcontracts Nos. 7446674, 7528983, and 7647045 between The Regents of the University of California and Surface Metrology Solutions LLC. Research at the Advanced Light Source at Lawrence Berkeley National Laboratory is supported by the Office of Science, Office of Basic Energy Sciences, and Material Science Division of the U.S. Department of Energy under Contract No. DE-AC02-05CH11231.

## DISCLAIMER



## REFERENCES

[1] V. V. Yashchuk, N. A. Artemiev, I. Lacey *et al.*, "A new X-ray optics laboratory (XROL) at the ALS: Mission, arrangement, metrology capabilities, performance, and future plans", Proc. SPIE **9206,** pp**.** 92060I/1-19 (2014) 10.1117/12.2062042

[2] I. Lacey, and V. V. Yashchuk, "Characterization of Groove Density Variation of VLS gratings with ALS XROL LTP-II in different operation modes", Proc. SPIE **11492,** pp**.** 114920D/1-16 (2020) 10.1117/12.2568705

[3] S. M. Nikitin, G. S. Gevorkyan, W. R. McKinney *et al.*, "New twist in the optical schematic of surface slope measuring long trace profiler", in *Advances in Metrology for X-Ray and EUV Optics VII*, Proc. SPIE **10385,** pp**.** 103850I-1-17 (2017) 10.1117/12.2274400

[4] J. L. Kirschman, E. E. Domning, W. R. McKinney *et al.*, "Performance of the upgraded LTP-II at the ALS Optical Metrology Laboratory", Proc. SPIE **7077,** pp**.** 70770A/1-12 (2008)

[5] P. Z. Takacs, I. Lacey, and V. V. Yashchuk, "Raytracing the long trace profiler", in *Advances in Metrology for X-Ray and EUV Optics IX*, Proc. SPIE **11492,** pp**.** 1149204 (2020) 10.1117/12.2569751

[6] *Zemax OpticStudio*, Zemax/An Ansys Company, ver. 20.2.1,

[7] S. C. Irick, W. R. McKinney, D. L. Lunt *et al.*, "Using a straightness reference in obtaining more accurate surface profiles from a long trace profiler for synchrotron optics," Review of Scientific Instruments*,* 63 (1), pp. 1436-1438 (1992)

[8] P. Z. Takacs, and S. Qian, "Accuracy Limitations in Long-Trace Profilometry," AIP Conference Proceedings*,* 705 (1), pp. 831-834 (2004) doi: 10.1063/1.1757924

[9] M. Grindel, Private communication, (1991)

[10] P. Z. Takacs, "Slope profilometry of grazing incidence optics" presented at *International Workshop on Extreme Optics and Sensors*, Ikebukuro, Tokyo, Japan,(14-17 January 2003), in "International Progress on Advanced Optics and Sensors", ed. H. Ohmori and H. M. Shimizu, pp. 255-262, Universal Academy Press, Tokyo, Japan, ISBN: 4-946443-76-2, (2003).

[11] S. C. Irick, W. R. McKinney, D. L. T. Lunt *et al.*, "Using a straightness reference in obtaining more accurate surface profiles," Rev. Sci. Instrum. 63, 1436-1438.

[12] J. S. Stroud, "Striae quality grades for optical glass," Opt. Eng.*,* 42 (6), pp. 1618-1624 (2003) doi: 10.1117/1.1571549

[13] Schott, Technical Information, **TIE-25**, "Striae in optical glass", (June 2006), https://www.schott.com/en-us/products/optical-glass-p1000267/downloads

[14] Schott, Technical Information, **TIE-26**, "Homogeneity of optical glass", (February 2016), https://www.schott.com/en-us/products/optical-glass-p1000267/downloads

[15] P. Z. Takacs, and S. Qian, "Sub-microradian error sources in pencil beam interferometry", in *Optical Manufacturing and Testing V*, Proc. SPIE **5180,** pp**.** 377-384 (2003)

[16] *Mathematica*™, Wolfram Research, Inc., ver. 13.2, Champaign, IL, (2022)